

## Remote Sensing of Precipitable Water over the Oceans from Nimbus 7 Microwave Measurements

C. PRABHAKARA, H. D. CHANG<sup>1</sup> AND A. T. C. CHANG

*Goddard Laboratory for Atmospheric Sciences, NASA/Goddard Space Flight Center, Greenbelt, MD 20771*

(Manuscript received 24 April 1981, in final form 10 October 1981)

### ABSTRACT

Nimbus 7 Scanning Multichannel Microwave Radiometer (SMMR) brightness temperature measurements in the 21 and 18 GHz channels are used to sense the precipitable water in the atmosphere over oceans. The difference in the brightness temperature ( $T_{21} - T_{18}$ ), both in the horizontal and vertical polarization, is found to be essentially a function of the precipitable water in the atmosphere. An equation, based on the physical considerations of the radiative transfer in the microwave region, is developed to relate the precipitable water to ( $T_{21} - T_{18}$ ). It is shown from theoretical calculations that the signal ( $T_{21} - T_{18}$ ) does not suffer severely from the noise introduced by variations in sea surface temperature, surface winds and liquid water content in non-raining clouds. The rms deviation between the estimated precipitable water from SMMR data and that given by the closely coincident ship radiosondes is about  $0.25 \text{ g cm}^{-2}$ .

Global maps of precipitable water over oceans derived from SMMR data reveal several salient features associated with ocean currents and the large-scale general circulation in the atmosphere.

### 1. Introduction

Water vapor in the atmosphere is an important constituent because it plays a significant role in the absorption and emission of radiative energy, and in the development of fog, clouds and precipitation. Remote sensing of this constituent on a global basis can be of aid in the understanding and prediction of weather and climate processes. Because of the low vertical resolution ( $\sim 3 \text{ km}$ ) obtainable with present passive remote sensing techniques, the accuracy of the derived vertical profile of water vapor is poor (Conrath, 1969; Smith and Woolf, 1976). However, the vertically integrated water vapor amount (precipitable water), particularly over water bodies, can be determined fairly accurately.

Precipitable water in the atmosphere over the oceans is a useful parameter which indicates the dynamic state of the atmospheric boundary layer. When low-level convergence is present in the atmosphere, a deep convective layer is formed resulting in a relatively large amount of precipitable water. On the other hand, when stable conditions prevail, such as those associated with low-level inversions, a dry layer above the inversion is formed and the precipitable water in the atmosphere consequently is reduced. In a recent study using Nimbus 4 Infrared Interferometer Spectral measurements, Prabhakara *et al.* (1979) have derived precipitable water over the

global oceans for each season, and thereby inferred the structure of the atmospheric boundary layer.

In the remote sensing of sea surface temperatures from infrared window radiance measurements, it is necessary to apply a correction for atmospheric water vapor absorption. Satellite sensing of the precipitable water can thus help improve the accuracy of the sea surface temperature measurement.

Remote sensing of the precipitable water over the global oceans utilizing microwave measurements from Nimbus 5 and Nimbus 6 has been demonstrated, among others by Staelin *et al.* (1976), Chang and Wilheit (1979) and Grody *et al.* (1980). The capability of microwave remote sensing through non-precipitating cloud is particularly valuable in getting global information on a time scale of about a week or less. The retrieval techniques used in these studies depend either on multiple regression, or on an approximation to the radiative transfer formalism. These methods have yielded an rms error in the estimated precipitable water of  $\sim 0.45 \text{ g cm}^{-2}$ .

The Nimbus 7 SMMR has two channels closely spaced in the spectrum, at 18 and 21 GHz (see Fig. 2), located on one side of the weak water vapor line centered at 22.235 GHz. The difference between the brightness temperature in these two channels yields a measure of the absorption strength of this weak water vapor line. Since the absorption strength of a weak line is proportional to the amount of absorbing gas (Plass, 1960), we can relate the brightness temperature difference to the precipitable water in the

<sup>1</sup> Computer Sciences Corporation, Silver Spring, MD.

TABLE 1. Comparison of remotely sensed precipitable water versus ship radiosonde measurements. A systematic bias of 8.5 K has been removed from all values of  $T_{21} - T_{18}$ .

Case no.	Date	Latitude	Longitude	$(T_{21} - T_{18})_v$ (K)	$w$ ( $\text{g cm}^{-2}$ )		$\Delta w$
					SMMR	Radiosonde	
1	10/25/78	36°N	22.9°W	31.4	3.60	3.29	0.31
2	10/25/78	52.8°N	35.5°W	30.6	3.48	3.43	0.05
3	10/25/78	29°N	135°E	31.5	3.48	3.34	0.14
4	10/26/78	50°N	145°W	15.3	1.17	1.04	0.13
5	10/26/78	52.8°N	35.5°W	24.9	2.58	3.02	-0.44
6	10/26/78	36°N	27.8°W	30.1	3.39	3.43	-0.04
7	10/28/78	66°N	2°E	10.1	0.54	0.67	-0.13
8	10/31/78	52.8°N	35.5°W	11.8	0.76	0.84	-0.08
9	11/5/78	50°N	145°W	21.4	2.07	2.34	-0.27
10	11/5/78	38.8°N	134.7°E	14.8	1.15	1.36	-0.21
11	11/6/78	66°N	2°E	10.2	0.56	0.55	0.01
12	2/15/79	47°N	17°W	15.9	1.3	1.15	0.15
13	2/15/79	66°N	2°E	11.5	0.74	0.7	0.04
14	2/15/79	50°N	145°W	10.8	0.63	0.62	0.01
15	2/15/79	57°N	20°W	12.3	0.82	1.11	-0.29
16	2/17/79	57°N	20°W	22.2	2.18	1.94	0.24
17	2/17/79	46.5°S	20.3°E	18.5	1.65	1.15	0.5
18	2/19/79	5.5°S	65.3°E	37.5	4.66	4.69	-0.03
19	2/19/79	50°N	145°W	16.0	1.31	1.3	0.01
20	2/21/79	11.8°S	65.2°E	38.2	4.6	4.84	-0.24
21	2/23/79	57°N	20°W	18.4	1.64	1.37	0.27
22	2/23/79	37°S	155.3°E	22.6	2.24	2.15	0.09
23	2/23/79	38.2°S	24.1°E	24.5	2.53	2.37	0.16
24	2/23/79	9.1°N	110.1°E	31.7	3.65	3.86	-0.21
25	2/25/79	4.9°N	30°W	34.3	4.09	4.7	-0.61
26	2/25/79	47°N	17°W	19.3	1.76	1.58	0.18
27	2/25/79	23°S	66.3°E	39.4	5.02	4.88	0.14
28	2/25/79	32.4°S	37.1°E	31.3	3.6	2.89	0.71

atmosphere. The retrieval technique developed in this study differs from the previous ones in this respect. This method is applied to the Nimbus 7 SMMR observations made over ship stations (see Table 1) that had radiosonde measurements. The satellite-sensed precipitable water agrees with that given by the radiosonde measurements to within an rms error of  $0.25 \text{ g cm}^{-2}$ .

## 2. Theoretical background

In the microwave region, spanning the SMMR frequencies from about 6 to 37 GHz, the principal absorber in the atmosphere is water vapor. In addition liquid water droplets contained in non-raining clouds, smaller than  $\sim 100 \mu\text{m}$  in radius, produce some absorption which increases approximately as the square of the frequency. This Rayleigh approximation which holds well for droplets  $\leq 100 \mu\text{m}$  starts to break down for large raindrops and Mie scattering gains importance (Gunn and East, 1954). The wind at the surface of the ocean changes the roughness of the water and thereby the surface emissivity, and, in addition, at wind speeds above  $\sim 7 \text{ m s}^{-1}$  white caps are formed which markedly affect the sea surface emissivity. These physical effects have been dis-

cussed in the earlier studies of Wilheit *et al.* (1975), Wilheit (1978), Chang and Wilheit (1979) and Staelin *et al.* (1976). In this study an attempt is made to take advantage of the known physics and arrive at an algorithm that improves the estimation of precipitable water over the oceans.

The radiative transfer formalism presented by Chang and Wilheit (1979) is adopted in this investigation. In this treatment the emissivity of the smooth sea surface has been calculated from the dielectric constant using the Fresnel relations (Jackson, 1962). The dielectric constant data of Lane and Saxton (1952) are used in these calculations. Inasmuch as the dielectric constant depends on the wavelength of the radiation and the temperature of the water, the microwave emissivity of the sea surface changes as a function of these variables.

In Fig. 1 the emissivity, in the vertical and horizontal polarization of the smooth sea surface, calculated as a function of temperature, at different frequencies of SMMR is shown. The approach taken by Gaut (1968) for the absorption coefficient of water vapor is adopted. Weak absorption due to molecular oxygen in the atmosphere at frequencies below 45 GHz is also taken into account. The ra-

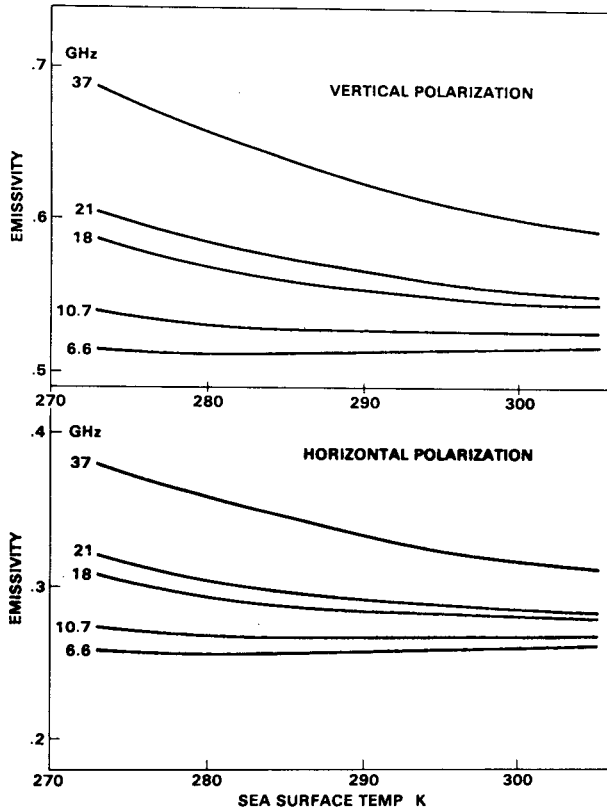


FIG. 1. Variation of smooth sea surface emissivity as a function of temperature for SMMR frequencies.

diative transfer equation in the microwave region can be written as

$$T_{B\nu} = T_0\epsilon_\nu\tau_{0\nu} + \int_{\tau_{0\nu}}^1 T(P)d\tau_\nu(P) + R_\nu\tau_{0\nu} \int_{\tau_{0\nu}}^1 T(P)d\tau_\nu^!(P), \quad (1)$$

where  $\nu$  is the frequency,  $T_{B\nu}$  the brightness temperature at the top of the atmosphere measured by the satellite sensor,  $P$  the pressure,  $T_0$  and  $T(P)$  are the temperature at surface and at pressure level  $P$ , respectively, and  $\tau_{0\nu}$  and  $\tau_\nu(P)$  are the transmission of the atmosphere from the surface and from any pressure level  $P$  to the satellite respectively, along a direction  $50^\circ$  with respect to the local vertical.  $\tau_\nu^!(P)$  is the transmission of the atmosphere from any pressure level  $P$  to the surface along a direction of  $50^\circ$  with respect to the local vertical.  $\epsilon_\nu$  is the surface emissivity and  $R_\nu$  the reflectivity of the surface. Furthermore,  $\epsilon_\nu + R_\nu = 1$ . The first term in the transfer equation represents the surface emission, the second term the atmospheric emission, and the third term corresponds to the atmospheric radiation reflected at the surface and then transmitted to the satellite sensor. The sea surface acts like a specular reflector

under calm conditions; however, when the surface is disturbed by high winds associated with storms, the sea surface approaches the characteristics of a Lambertian reflector. For average winds ( $5-10 \text{ m s}^{-1}$ ) over the sea one may assume surface roughness causes atmospheric emission from a distribution of zenith angles, peaking in the specular direction, to be reflected toward the radiometer (Rosenkrantz *et al.*, 1978). With these considerations we have adopted the following working approximation. The mean atmospheric emission, averaged over all the zenith angles, incident at the surface is reflected along a direction  $50^\circ$  with respect to the local vertical. This corresponds to the viewing geometry of the satellite radiometer. The mean incident radiation obtained in the above fashion approximates the emission from a zenith angle of about  $50^\circ$ . As such the procedure adopted here represents nearly a specular reflection.

Using Eq. (1), the brightness temperature spectrum between 6.6 and 37 GHz of the vertical polarized component of the radiation for a tropical atmosphere over the oceans with  $3.42 \text{ g cm}^{-2}$  of precipitable water is calculated (see Fig. 2.). This spectrum clearly reveals the shape of the weak water vapor line at 22.235 GHz. The spectral position of the various SMMR channels is shown. The brightness temperatures that would result in the absence of atmosphere is shown by a line labeled  $\epsilon_\nu T_s$ , where the surface temperature  $T_s = 298.6 \text{ K}$ . Shown in the same figure is a spectrum produced by the addition of a cloud between 1 and 2 km above the surface and containing  $50 \text{ mg cm}^{-2}$  of liquid water droplets ( $<100 \mu\text{m}$  in size). From this figure one can see that the brightness temperatures in all of the SMMR channels (6.6, 10.7, 18, 21, 37 GHz) are affected by the liquid water in clouds. In this case, the absorption due to liquid water is weak at 18 and 21 GHz in comparison with that due to water vapor. Furthermore, the liquid water absorption increases by 36% (using the Rayleigh approximation) in going from 18 to 21 GHz, while the absorption due to water vapor increases by a factor of 4. Mainly because of this reason, as will be shown in more detail later, the difference in brightness temperature ( $T_{21} - T_{18}$ ) remains approximately the same in the presence of a typical fair weather cloud containing  $<100 \text{ mg cm}^{-2}$  of liquid water in a column (Stephens, 1978). In addition, by taking the difference  $T_{21} - T_{18}$  we can practically eliminate the dependence on the surface temperature. This is illustrated in Fig. 3 where the variation in brightness temperatures  $T_{21}$  and  $T_{18}$  as a function of the surface temperature is shown. These brightness temperatures were computed by choosing one particular model atmosphere in which only the surface temperature was changed over a range of  $20^\circ\text{C}$ . The signal  $T_{21} - T_{18}$  changes by only  $0.6^\circ\text{C}$  over this wide range of surface temperatures.

On account of the reasons mentioned above and

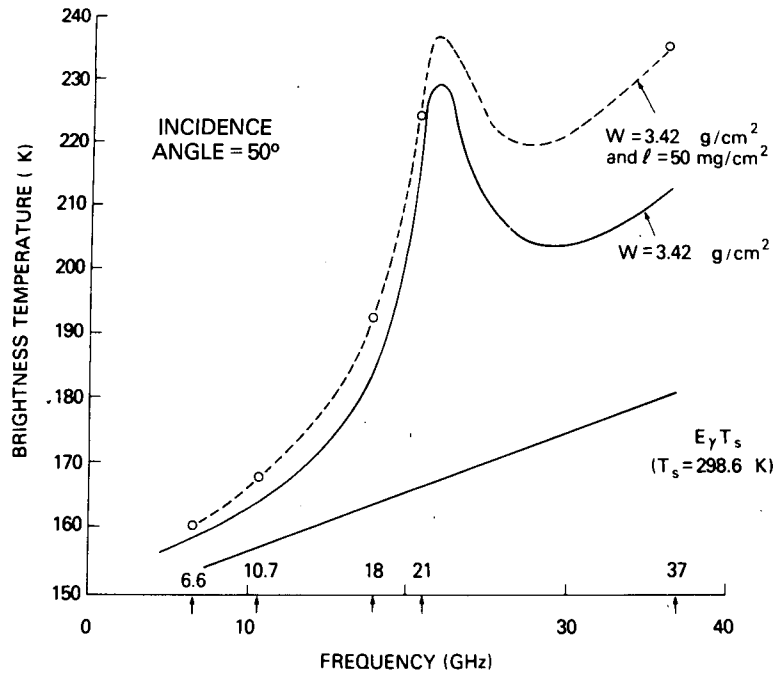


FIG. 2. Brightness temperature spectra between 6 and 37 GHz for (1) no atmosphere (solid line); (2) a tropical model atmosphere with  $3.42 \text{ g cm}^{-2}$  of precipitable water (solid curve); and (3) addition of  $50 \text{ mg cm}^{-2}$  of cloud liquid water to case 2 (dashed curve).

for its simplicity the signal  $T_{21} - T_{18}$  is examined in detail for water vapor sensing. Wilheit and Chang (1980), in their multiple regression analysis, also find that the information contained in the brightness tem-

perature measurements at 18 and 21 GHz is optimal for water vapor sensing. The reason for this is made clear in the following discussion.

With the radiative transfer equation we can ex-

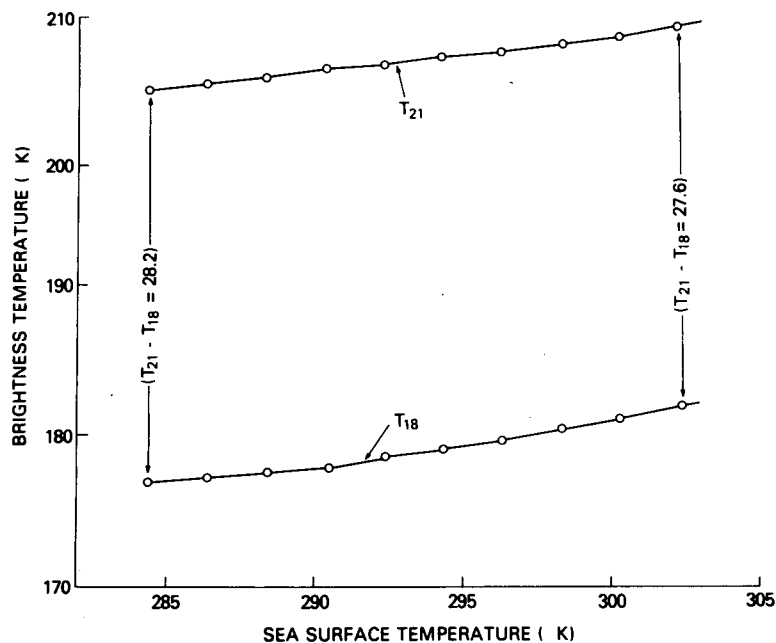


FIG. 3. Brightness temperature variation at 18 and 21 GHz in the vertical polarization as a function of sea surface temperature, based on theoretical calculations.

TABLE 2. Numerical values of the first, second and third terms in Eq. (2) for a sample of atmospheric cases over oceans.

$T_s$ (K)	$w$ (g cm <sup>-2</sup> )	Term in Eq. (2)				$(T_{21} - T_{18})_0$ (K)
		(1) (K)	(2) (K)	(3) (K)	(1 + 3) (K)	
278.0	0.96	-3.1	12.1	4.1	+1.0	13.1
293.6	2.06	-11.5	24.9	8.5	-3.0	21.9
292.8	3.54	-22.1	42.6	12.3	-9.8	32.8
298.8	4.26	-26.1	48.6	13.7	-12.4	36.3

press the brightness temperature difference  $T_{21} - T_{18}$  as

$$\begin{aligned}
 (T_{21} - T_{18}) = & T_0(\epsilon_{21}\tau_{021} - \epsilon_{18}\tau_{018}) \\
 & + \int_{\tau_0}^1 T(P)d[\tau_{21}(P) - \tau_{18}(P)] \\
 & + \left[ R_{21}\tau_{021} \int_{\tau_0}^1 T(P)d\tau_{21}^1(P) \right. \\
 & \left. - R_{18}\tau_{018} \int_{\tau_0}^1 T(P)d\tau_{18}^1(P) \right]. \quad (2)
 \end{aligned}$$

In this equation the first and the last terms depend on the surface properties. When appropriate values of the parameters are introduced the first and last terms have opposite sign and tend to cancel one another. The numerical values of the first, second and third terms in Eq. (2) corresponding to a few atmospheric cases, over oceans, are listed in Table 2 to demonstrate this point. This happens in both the vertical and horizontal polarizations. In this study, as will be discussed in Section 4, we have utilized the

vertical polarization measurements for our remote sensing. For this reason in Table 2 only the vertical polarization calculations are shown. The second term which represents the atmospheric emission, as shown in Table 2, makes the largest contribution to  $T_{21} - T_{18}$ . Since we are interested in obtaining the information on water vapor contained in the atmosphere this is a very desirable condition. In order to demonstrate this interesting behavior, we have calculated the brightness temperatures, using detailed radiative transfer formalism, for 50 atmospheric cases ranging from high latitudes to the equator. These atmospheric cases correspond to radiosonde measurements made by ship stations. In Fig. 4, calculations of  $T_{21} - T_{18}$  are shown as a function of the precipitable water in the atmosphere, for both vertical and horizontal polarizations. Also shown is the atmospheric emission term, which is common to both the vertical and horizontal polarizations. The atmospheric term lies between the curves for the two polarizations and accounts for a substantial part of  $T_{21} - T_{18}$ . The small scatter in the neighboring values of the atmospheric emission and  $T_{21} - T_{18}$  in both polarizations shown in Fig. 4 suggests that these quantities depend principally on the precipitable water and only in a secondary way on the sea surface temperature and vertical profiles of temperature and water vapor.

At this point it is helpful to simplify (2) for the purposes of remote sensing. This can be done by approximating the integrals in the equation by choosing equivalent radiative temperature of the atmosphere. Further, since the emissivity at 18 and 21 GHz differs only slightly (see Fig. 1), we can choose a mean emissivity  $\bar{\epsilon}$  for both the channels. With these ap-

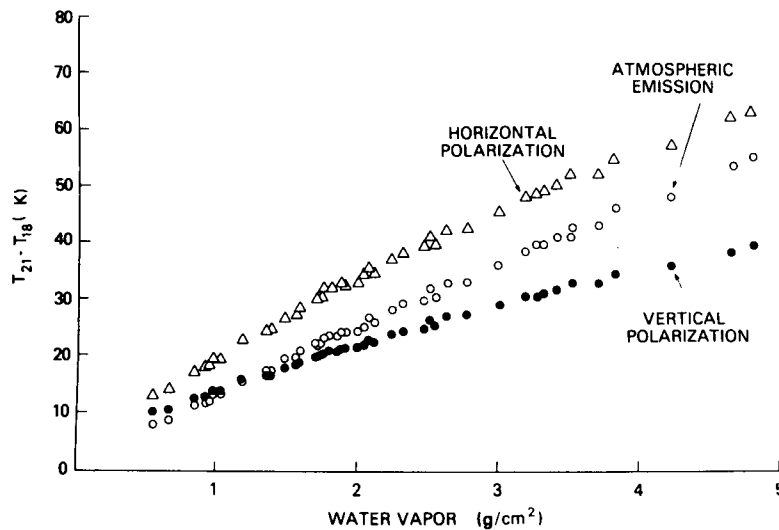


FIG. 4. Theoretical relationship between  $(T_{21} - T_{18})$ , in vertical and horizontal polarization, and precipitable water in the atmosphere. Atmospheric emission is calculated according to second term in Eq. (2).

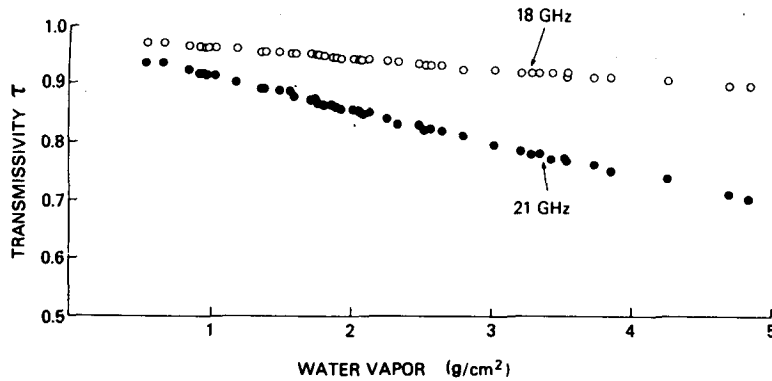


Fig. 5. Transmissivity as a function of precipitable water in the atmosphere at 18 and 21 GHz.

proximations we get

$$(T_{21} - T_{18}) \approx \tilde{\epsilon} T_0 (\tau_{0_{21}} - \tau_{0_{18}}) - \bar{T} (\tau_{0_{21}} - \tau_{0_{18}}) + (1 - \tilde{\epsilon}) \bar{T}' (\tau_{0_{21}} - \tau_{0_{18}}) [1 - (\tau_{0_{21}} + \tau_{0_{18}})], \quad (3)$$

where  $\bar{T}$  and  $\bar{T}'$  are equivalent radiative temperatures of the upwelling and downwelling radiation. As the vertical distribution of water vapor is heavily weighted by the lower layers of the atmosphere we may approximate

$$T_0 \approx \bar{T} \approx \bar{T}'. \quad (4)$$

Substituting the approximations (4) into Eq. (3) we get

$$(T_{21} - T_{18}) \approx [(1 - \tilde{\epsilon}) \bar{T} (\tau_{0_{21}} + \tau_{0_{18}})] \times (\tau_{0_{18}} - \tau_{0_{21}}). \quad (5)$$

(a)

(b)

This equation is consistent with that derived by Grody (1976). The quantity (a) on the right side of the equation remains nearly a constant, from the equator to high latitudes (excluding sea ice), for realistic values of  $\tilde{\epsilon}$  (see Fig. 1),  $\tau_{18}$  and  $\tau_{21}$  (see Fig. 5) and  $\bar{T}$ . The reason for this is  $(1 - \tilde{\epsilon}) \bar{T}$  decreases from equator to pole while  $(\tau_{0_{21}} + \tau_{0_{18}})$  increases by about the same proportion.

This result suggests that one may seek a direct relationship between  $T_{21} - T_{18}$  and the transmission difference  $\tau_{0_{18}} - \tau_{0_{21}}$  of the water vapor  $w$  in the atmosphere, i.e.,

$$T_{21} - T_{18} = C_0 + C_1 \exp(-k_{O_x} m x) \times [\exp(-k_{18} w x) - \exp(-k_{21} w x)], \quad (6)$$

where  $C_0$  and  $C_1$  are constants to be determined from the theoretical calculations shown in Fig. 4.  $k_{O_x}$  is the effective absorption coefficient of oxygen at the central frequency of 19.5 GHz;  $k_{18}$  and  $k_{21}$  are ef-

fective absorption coefficients for water vapor at 18 and 21 GHz,  $m$  is the path length of molecular oxygen in the atmosphere, and  $x = \sec \theta$  where  $\theta = 50^\circ$  corresponds to the viewing geometry of SMMR on Nimbus 7. These  $k$  values are determined from transmission computations made for the 50 ship radiosonde soundings that were mentioned earlier. The transmissions as a function of  $w$  for the 21 and 18 GHz are shown in Fig. 5. The values of  $k_{18}$  and  $k_{21}$  estimated from Fig. 5 are equal to 0.0116 and 0.0438  $\text{cm}^2 \text{g}^{-1}$ , respectively. A value of  $\exp(-k_{O_x} m x) = 0.98$  is obtained from calculations. With these estimates we get the following equations to fit the calculated  $T_{21} - T_{18}$  shown in Figure 4 for the horizontal and vertical polarizations:

$$(T_{21} - T_{18})_V = 5.7 + 169 \times 0.98 \times [\exp(-k_{18} w x) - \exp(-k_{21} w x)], \quad (7)$$

$$(T_{21} - T_{18})_H = 6.1 + 289 \times 0.98 \times [\exp(-k_{18} w x) - \exp(-k_{21} w x)]. \quad (8)$$

Eqs. (7) and (8) fit the data shown in Fig. 4 to within 1 K over the range of 0.5 to 5  $\text{g cm}^{-2}$  of precipitable water.

From Eqs. (7) and (8) one notices that the precipitable water signal ( $T_{21} - T_{18}$ ) in the horizontal polarization is about 1.7 times larger than that in the vertical polarization essentially because of the difference in the surface emissivity for the two polarizations. One can take a linear combination of the two equations in an attempt to utilize the horizontal and vertical polarization measurements jointly.

### 3. Sources of error in the precipitable water estimation

The SMMR measurements at 18 and 21 GHz are available at a spatial resolution of 60 km. However, to reduce noise in the data we are utilizing mea-

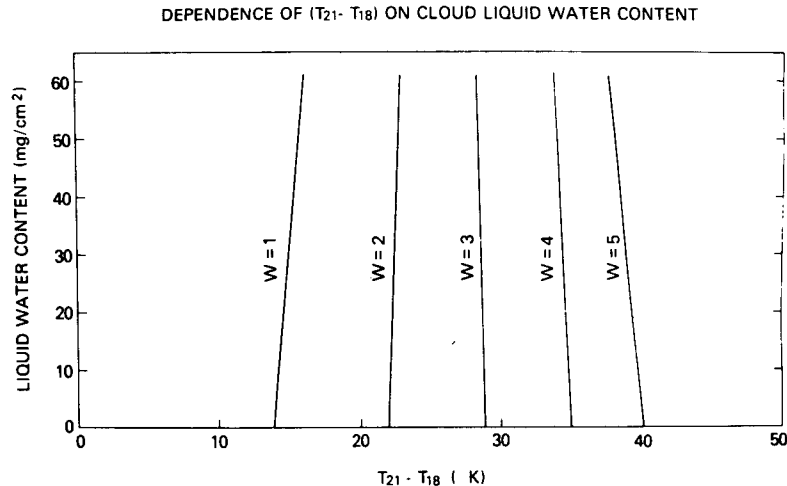


FIG. 6. Variation of  $(T_{21} - T_{18})$  in the vertical polarization, for a given precipitable water, in the presence of cloud liquid water content.

surements that represent a spatial average over a 156 km footprint.

The rms error in the SMMR 18 and 21 GHz brightness temperature measurement, in a field of view of 156 km, is estimated to be 0.5 K (Gloersen *et al.*, 1978). This will lead to an error of 0.7 K in  $T_{21} - T_{18}$  which corresponds to an error of 0.1 g cm<sup>-2</sup> of precipitable water. In order to estimate the error introduced by liquid water in the clouds we have calculated the brightness temperatures  $T_{21}$  and  $T_{18}$  for the set of 50 radiosonde profiles mentioned earlier, including liquid water clouds, containing 0, 25 and 50 mg cm<sup>-2</sup> of the liquid distributed between 1 and 2 km above the surface. In Fig. 6 the calculated  $(T_{21} - T_{18})$  obtained from such calculations is shown as a function of the liquid water in the cloud. The isopleths of precipitable water  $w$  shown in the figure reveal the sensitivity of the estimated  $w$  to  $(T_{21} - T_{18})$  in the presence of liquid water droplets. It is seen from the figure that below 2.7 g cm<sup>-2</sup>,  $w$  is overestimated in the presence of clouds. The opposite effect is seen above  $\sim 2.7$  g cm<sup>-2</sup>. This error could be as large as 0.3 g cm<sup>-2</sup> when the cloud liquid water content is 50 mg cm<sup>-2</sup>. The winds at the surface increase the surface emissivity of the ocean and thus affect the satellite-measured brightness temperatures. Taking Wilheit's (1979) model of the surface brightness change produced by wind at different wavelengths, we find that  $(T_{21} - T_{18})$  will be systematically reduced by the surface winds. This results in a systematic underestimation of precipitable water. A surface wind of 30 m s<sup>-1</sup> results in an underestimation of precipitable water by  $\sim 10\%$ . Further, this effect is almost linearly proportional to the wind speed.

From the discussion of these errors we see that the error introduced by substantial liquid water in the

clouds and high winds could be appreciable. However, the errors introduced under average conditions of wind (10 m s<sup>-1</sup>) and clouds (assumed to contain  $<30$  mg cm<sup>-2</sup>) should lead to an error of  $\sim 0.2$  g cm<sup>-2</sup>. Now if we consider all the sources of error (instrument noise, surface winds and clouds), one can expect an error of  $\sim 0.3$  g cm<sup>-2</sup>.

#### 4. Comparison with radiosonde measurements

For the purpose of comparison an independent sample of 28 coincident ship radiosonde measurements and Nimbus 7 SMMR observations were obtained. Coincidence is assumed when the center of the satellite field of view is within 1° latitude and longitude of the ship location and when the time difference between the ship and the satellite observations does not exceed one day. The satellite data used in this study have a foot print size of 156 km.

The Nimbus 7 SMMR data have some systematic calibration bias. We find the bias in the vertical polarization measurements to be considerably smaller than that in the horizontal polarization. For this reason we have restricted our study to the vertical polarization data. In order to assess this systematic bias, the brightness temperatures are calculated at the SMMR frequencies utilizing the detailed radiative transfer formalism described earlier. A selected set of coincident ship radiosonde data different from the sample mentioned above is used for this purpose. Winds at the surface and liquid water in the cloud, if any, are not considered. When  $(T_{21} - T_{18})$  computed in this fashion is compared with that observed by SMMR it is found that the satellite measurements yield a value that is systematically larger by 8.5 K. After removing this bias, precipitable water is estimate from SMMR data for the sample of 28 coin-

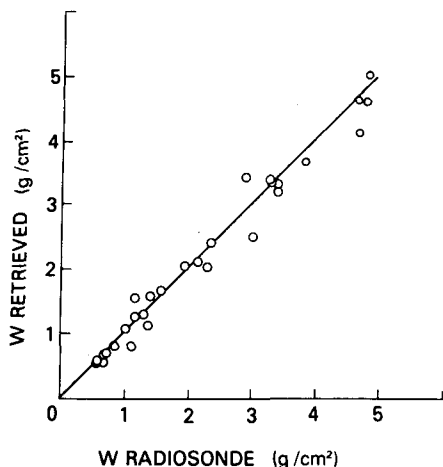


FIG. 7. Comparison of ship radiosonde measured precipitable water with that estimated from Nimbus-7 SMMR data.

cident cases, with the help of Eq. (7). In Table 1 the relevant data observed from the satellite and ship radiosonde measurements are presented.

In Fig. 7 these estimates of  $w$  from SMMR are compared with those of radiosondes. The agreement between the two sets of data is good yielding an rms error of  $0.25 \text{ g cm}^{-2}$ . This error is not inconsistent with the error analysis presented in the previous sec-

tion. Wilheit and Chang (1980) developed a multiple regression relationship between the precipitable water in the atmosphere and the brightness temperatures in the vertical and horizontal polarizations at 18 and 21 GHz. A test of their method with the present sample of radiosonde data yields an rms error in the precipitable water of  $0.3 \text{ g cm}^{-2}$  which is not significantly larger than the value obtained in the present study.

The regression method of Grody *et al.* (1980) based on the measurements of Scanning Microwave Spectrometer (SCAMS) on Nimbus 6 at 22 and 31 GHz yielded an error of about  $0.45 \text{ g cm}^{-2}$ . This somewhat larger error could be due to the large field of view of SCAMS as compared to that of SMMR.

**5. Description of precipitable water over global oceans**

Utilizing the Nimbus 7 SMMR measurement for a period of two months (25 October–25 November 1978 and 15 February–17 March 1979) we have derived eight global maps of precipitable water on a weekly basis. Two monthly mean global maps, one for 25 October–25 November 1978, and another for 15 February–17 March 1979, are also generated. These maps are presented in a study by Prabhakara *et al.* (1981). In Fig. 8 one global map of the pre-

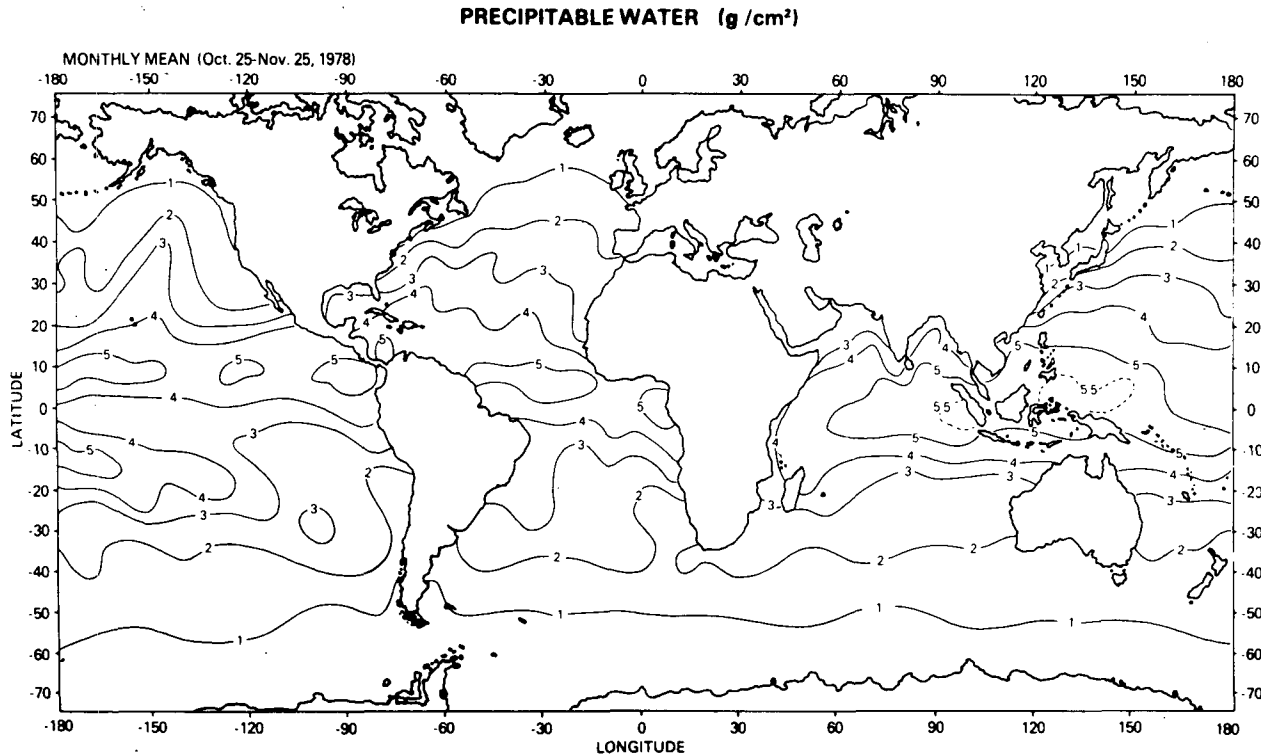


FIG. 8. Distribution of precipitable water in the atmosphere, over the global oceans, derived from Nimbus-7 SMMR data for the period 25 October–25 November 1978.



precipitable water corresponding to 25 October–25 November 1978 is presented as an example.

An examination of the map of precipitable water reveals minima in the eastern parts of subtropical Atlantic and Pacific Oceans in the Northern and Southern Hemispheres. These are regions of large-scale subsidence. The relatively dry tongue associated with the subsidence motion (Bjerknes, 1969) in the eastern equatorial Pacific is clearly revealed. The maxima of precipitable water associated with the Intertropical Convergence Zone (ITCZ) can be noticed both to the north and south of the equator. Most of these characteristics were revealed in the earlier studies using the microwave and infrared satellite data.

The SMMR data have enabled us to use a field of view of 156 km which is significantly better than the 250 km field of view of the Nimbus 6 SCAMS used in the earlier microwave water vapor sensing studies (Grody, 1978; Grody *et al.*, 1980). Also the rms error of the present method is  $0.25 \text{ g cm}^{-2}$  compared to  $0.45 \text{ g cm}^{-2}$  of the earlier microwave methods. For these reasons we are able to obtain finer information on the global distribution of precipitable water. The isopleths of the precipitable water show a marked orientation along the direction of flow of warm ocean currents such as the Gulf Stream and the Kuroshio. The gradient of precipitable water is in a direction normal to such warm ocean currents, suggesting that an increase in precipitable water accompanies an increase in sea surface temperature. This is observed generally on the east coast of the continents. Similarly, the influence of the cold ocean currents, such as the California and the Peruvian currents on continental west coasts, can be seen.

## 6. Conclusions

Nimbus 7 SMMR microwave brightness temperature measurements in the 18 and 21 GHz channels are found to be very useful for remote sensing of precipitable water in the atmosphere over the oceans. The signal obtained by taking the difference between the measured brightness temperature in two channels,  $T_{21} - T_{18}$ , greatly reduces the noise introduced by the variations in surface temperature, and the atmospheric profiles of the temperature and water vapor. Non-raining clouds containing liquid water droplets amounting to less than  $30 \text{ mg cm}^{-2}$  and light winds at the surface, less than  $10 \text{ m s}^{-1}$ , constitute a source of error of about  $0.3 \text{ g cm}^{-2}$ . However, heavy winds and clouds containing substantial amounts of liquid water can introduce substantial error. With the exception of the surface winds, the infrared remote-sensing methods to estimate precipitable water in the atmosphere depend sensitively on the sea surface temperature, temperature and water vapor profiles, and clouds of all kinds. Incorrect specification

of these variables can lead to significant errors in the infrared methods. Thus, considering the merits of the infrared and microwave remote-sensing techniques to retrieve precipitable water in the atmosphere, over the oceans, it appears that the microwave approach is preferable for both accuracy and spatial coverage. On the other hand, work done by Smith and Woolf (1976) showed that the vertical profile of water vapor can be inferred with a better accuracy when both infrared and microwave measurements are available. As the water vapor information is important in exploring the dynamics of the lowest layers in the atmosphere over the oceans, simultaneous measurements of infrared and microwave regions will be valuable for weather and climate studies.

*Acknowledgment.* We are thankful to Dr. T. T. Wilheit for his suggestions and comments which have enabled us to improve this paper.

## REFERENCES

- Bjerknes, J., 1969: Atmospheric teleconnections from the equatorial Pacific. *Mon. Wea. Rev.*, **97**, 163–172.
- Chang, A. T. C., and T. T. Wilheit, 1979: Remote sensing of atmospheric water vapor, liquid water, and wind speed at the ocean surface by passive microwave techniques from Nimbus 5 satellite. *Radio Sci.*, **14**, 793–803.
- Conrath, B. J., 1969: On the estimation of relative humidity profiles from medium resolution infrared spectra obtained from a satellite. *J. Geophys. Res.*, **74**, 3347–3361.
- Gaut, N. E., 1968: Studies of atmospheric water vapor by means of passive microwave techniques. Tech. Rep. 467, Res. Lab. Electron., MIT.
- Gloerson, P., and L. Hardis, 1978: Scanning multichannel microwave radiometer (SMMR) experiment. *Nimbus 7 Users' Guide*, C. R. Madrid, Ed., NASA/Goddard Space Flight Center, Greenbelt, MD.
- Grody, N. C., 1976: Remote sensing of atmospheric water content from satellites using microwave radiometry. *IEEE Trans. Antennas Propagat.*, **AP-24**, 155–162.
- , 1978: High resolution passive microwave satellite applications to synoptic meteorology and climatology. Application Review Panel Report, D. H. Staelin and P. W. Rosenkranz, Eds., MIT Res. Lab. Electron., No. 6, 1–6.
- , A. Gruber and W. C. Shen, 1980: Atmospheric water content over the tropical Pacific derived from the Nimbus-6 Scanning Microwave Spectrometer. *J. Appl. Meteor.*, **19**, 986–996.
- Gunn, L. L. S., and T. W. R. East, 1954: The microwave properties of precipitation particles. *Quart. J. Roy. Meteor. Soc.*, **80**, 522–545.
- Halberstam, I., 1980: Some considerations in the evaluation of Seasat-A Scatterometer (SASS) Measurements. *J. Phys. Oceanogr.*, **10**, 623–632.
- Jackson, J. D., 1962: *Classical Electrodynamics*. Wiley (see p. 219).
- Lane, J. A., and J. A. Saxton, 1952: Electrical properties of sea water. *Wireless Engineering*, **29**, 269–275.
- Prabhakara, C., H. D. Chang and A. T. C. Chang, 1981: Remote sensing of precipitable water over the oceans from Nimbus 7 microwave measurements. Tech. Memo., NASA/Goddard Space Flight Center, Greenbelt, MD.
- , G. Dalu, R. C. Lo and N. R. Nath, 1979: Remote sensing of seasonal distribution of precipitable water vapor over the oceans and the inference of boundary-layer structure. *Mon. Wea. Rev.*, **107**, 1388–1401.

- Plass, G. N., 1960: Useful representations for measurements of spectral band absorption. *J. Opt. Soc. Amer.*, **50**, 868-875.
- Rosenkranz, P. W., D. H. Staelin and N. C. Grody, 1978: Typhoon June (1975) viewed by a scanning microwave spectrometer. *J. Geophys. Res.*, **83**, 1857-1868.
- Smith, W. L., and H. M. Woolf, 1976: The use of eigenvectors of statistical covariance matrices for interpreting satellite sounding radiometer observations. *J. Atmos. Sci.*, **33**, 1127-1140.
- Staelin, D. H., K. F. Kunzi, R. L. Pettyjohn, R. K. L. Poon, R. W. Wilcox and J. W. Waters, 1976: Remote sensing of atmospheric water vapor and liquid water with the Nimbus 5 microwave spectrometer. *J. Appl. Meteor.*, **15**, 1204-1214.
- Stephens, G. L., 1978: Radiation profiles in extended water clouds. I: Theory. *J. Atmos. Sci.*, **35**, 2111-2122.
- Wilheit, T. T., 1978: A review of applications of microwave radiometry to oceanography. *Bound. Layer Meteor.*, **13**, 277-293.
- , 1979: A model for the microwave emissivity of the oceans' surface as a function of wind speed. *IEEE Trans. Geosci. Electron.*, **GE-17**, 244-249.
- , A. T. C. Chang, M. S. V. Rao, E. B. Rodgers and J. S. Theon, 1977: A satellite technique for quantitatively mapping rainfall rates over the oceans. *J. Appl. Meteor.*, **16**, 551-560.
- , and A. T. C. Chang, 1980: An algorithm for retrieval of ocean surface and atmospheric parameters from the observations of the Scanning Multichannel Microwave Radiometer (SMMR). *Radio Sci.*, **15**, 525-544.